



Rovere, F., Barakos, G. N. and Steijl, R. (2021) Safety analysis of Rotors in Ground Effect. In: AIAA Aviation Forum 2021, 2-6 Aug 2021, ISBN 9781624106101 (doi:[10.2514/6.2021-2625](https://doi.org/10.2514/6.2021-2625))

The material cannot be used for any other purpose without further permission of the publisher and is for private use only.

There may be differences between this version and the published version. You are advised to consult the publisher's version if you wish to cite from it.

<http://eprints.gla.ac.uk/244602/>

Deposited on 24 June 2021

Enlighten – Research publications by members of the University of  
Glasgow

<http://eprints.gla.ac.uk>

# Safety analysis of Rotors In Ground Effect

F. Rovere <sup>\*</sup>, R. Steijl <sup>†</sup>, G. N. Barakos <sup>‡</sup>  
*CFD Laboratory School of Engineering, University of Glasgow.*

In this work, computational fluid dynamics is used to perform safety analyses of rotors operating in ground effect. Initially, the paper focuses on the evaluation and prediction of the outwash generated by a micro-rotor operating at different heights above the ground. Time-averaged outflow velocities are compared with experimental results. Then, the simulated flowfield was used for safety studies using the PAXman model and particle tracking methods. The aircraft weights have been studied, evaluating scaling factors to define how the helicopter weight can affect the outflow forces and the particle paths. The results show how the wake generated by heavier helicopters can lead to stronger forces on ground personnel and pushes the particles farther away from the rotor. Furthermore, the distance between the ground and the rotor has an influence on particle path, generating different dangerous scenarios for the aircraft crew and ground personnel.

Nomenclature			
Latin			
$\mathbf{u}$	Flowfield velocity vector, $m/s$	$D$	Rotor diameter, $m$
$\mathbf{u}_p$	Particle velocity vector, $m/s$	$d_p$	Particle diameter, $\mu m$
$\mathbf{u}_S$	Splash entrained particle velocity vector, $m/s$	$d_i$	Distance between particle and the $i$ -th cell centre, $m$
$\mathbf{u}_{Rp}$	Rebound particle velocity vector, $m/s$	$dF_{PAXman}$	$dF_{PAXman} = \frac{1}{2}\rho V_{rad}^2 dA, N$
$\mathbf{J}$	Impulsive Force Impact, $kgm/s$	$DL$	Disk loading, $N/m^2$
$A$	Bangold model constant	$E$	Total kinetic energy, $Kg(m/s)^2$
$a$	Speed of sound, $m/s$	$e$	Coefficient of resitution
$a_p$	Particle acceleration, $m/s^2$	$f$	Coloumb frictional force
$B$	Balistic coefficient, $kg/m^2$	$F_{PAXman}$	$F_{PAXman} = \int_{A_{PAXman}} df_{PAXman}, N$
$c$	Blade chord, $m$	$g$	Gravitational acceleration, $g = 9.81m/s^2$
$C_D$	Drag coefficient	$h_{PAXman}$	PAXman height scaled, $m$
$C_Q$	Rotor torque coefficient, $C_Q = \frac{Q}{\frac{1}{2}\rho_{\infty}V_{tip}^2\pi R^3}$	$M$	Mach number, $M = V_{tip}/a_{\infty}$
$C_T$	Thrust coefficient, $C_T = \frac{2DL}{\rho_{air}V_{tip}^2}$	$m_p$	Particle mass, $kg$
		$N_b$	Number of blades
		$N_s$	Number of ejected particles,
		$ps$	Plastic pressure of the soil, $N/m^2$
		$Q$	Rotor torque, $N \cdot m$

<sup>\*</sup>PhD Student - federico.rovere@glasgow.ac.uk

<sup>†</sup>Senior Lecturer - rene.steijl@glasgow.ac.uk

<sup>‡</sup>Professor - george.barakos@glasgow.ac.uk - Corresponding author

$R$	Rotor radius, $m$	$\Phi$	multivariate normal distribution for the emitted particle velocity
$r$	Radial coordinate along blade span, $m$	$\Psi$	Local azimuth angle, $deg$
$r_{max}$	Maximum distance traveled by the particle during $\Delta t$ , $m$	$\rho$	Density, $kg/m^3$
$Re$	Reynolds number, $Re = V_{tip}c/v_\infty$	$\sigma_{xx}, \sigma_{yy}, \sigma_{zz}$	Variance velocity components for gaussian distribution, $m/s$
$S_p$	Frontal particle area, $m^2$	$\theta_{75}$	Collective pitch at three-quarter radius, $deg$
$S_{rotor}$	Rotor disk area, $m^2$	<b>Super and sub scripts</b>	
$T$	Rotor thrust, $N$	$\infty$	Freestream value
$U$	Velocity x-component, $m/s$	$air$	Air
$u^*$	Friction velocity, $m/s$	$fs$	Full scale
$V$	Velocity y-component, $m/s$	$p$	Particle
$V_c$	Volume crater, $m^3$	$R$	Rebound particle
$v_i$	Hover induced velocity, $v_i = \frac{\sqrt{C_T}}{2}$	$ss$	Small scale
$v_{max}$	Highest value of radial velocity component, $m/s$	$tip$	Blade tip value
$V_{rad}$	Radial velocity component, $V_{rad} = U \cos(\Psi) + V \sin(\Psi)$ , $m/s$	<b>Acronyms</b>	
$u_i^*$	Wall friction velocity threshold, $m/s$	$CFD$	Computational Fluid Dynamics
<b>Greek</b>		$DVE$	Degraded Visual Environment
$\alpha_0$	Impacting particle angle, $deg$	$IGE$	In Ground Effect
$\beta$	Bangold model constant	$MTOW$	Maximum TakeOff Weight
$\epsilon_x, \epsilon_y$	Proportion of the velocity on wall plane component direction	$MUSCL$	Monotone Upstream Centred Schemes for Conservation Laws
$\mu_B$	Main velocity vector for gaussian distribution, $m/s$	$OGE$	Out of Ground Effect
$\nu$	Kinematic viscosity, $m^2/s$	$PIV$	Particle Image Velocimetry

## 1. Introduction

The flowfields generated by rotors operating In Ground Effect (IGE) are complex and unsteady. Furthermore, the result of the interaction between the rotor wake and the ground plane is the transition of the rotor induced flow from vertical (downwash) to radial flow (outwash). This can be a source of risk for ground personnel, equipment and landscape due to the forces generated by high outflow velocities. Furthermore, in case of brownout or whiteout the flowfield can interact with a loose sediment bed, uplifting particles all around the aircraft. The prediction of the outwash is fundamental for the safety of IGE operations [1], [2]. The downwash typically affects activities directly under the aircraft (like search and rescue operations), while the outwash impacts the surrounding environment like people, equipment and structures during landing and take-off. Rotor wakes IGE may also affect other aircraft operating nearby, and various works tried to define a 'safe zone' for wake encounters [3]. As already mentioned, brownout and whiteout may occur when a rotorcraft is operating in ground proximity, and are due to the interaction of the rotor wake with particles of a loose sediment bed such as sand, snow etc. This interaction can eventually uplift particles from the ground into the air flow. When operating in desert areas or in snowy regions, the number of particles entrained can

create a cloud around the rotorcraft. The main effect of this cloud of particles moving around the aircraft is on the pilot's visual environment. The rotorcraft structure and on-board equipment can also be affected. The lack of pilot visibility defines brownout and whiteout as Degraded Visual Environment (DVE) conditions. In recent years, efforts have been made to help pilots in these situations, developing sensors and advanced cockpit displays. Dynamic rollover and collisions with objects are common accidents due to the low visibility [4]. NATO collected data about mishaps due to brownout or whiteout in [5]. The US Air force lost 30 special operations aircraft and 60 crew members lost their lives during landing in desert environments since 1990. In the same report, the authors specify that the brownout cost to US services was \$100M/yr. Other NATO members experienced similar statistics. The occurrence of brownout is the most common cause of human factor mishaps during military operations [6]. Due to the complexity of these phenomena and the risks for safety that they may generate, rotor wakes have been studied using different approaches, from full-scale aircraft tests [2], to small-scale isolated rotors [7, 8]. In the first case, during experiments, it is possible to replicate the real operational conditions the aircraft may encounter in an operational scenario. In general, however, measurement techniques used in full-scale experiments, lack high resolution, and cannot provide a detailed view of the phenomena involved. On the other hand, small-scale studies can be performed in a laboratory, within a controlled environment using high resolution measuring techniques, such as Particle Image Velocimetry (PIV). However, due to the limited size of the rotors, Reynolds number is lower with respect to the full-scale case, leading to some differences in the flowfield behaviour.

In the present work, computational fluid dynamics (CFD) is used to perform safety analysis of rotors operating IGE. Initially, experimental data of a micro-rotor, operating IGE at different heights above the ground, are compared with CFD results. The simulated test case was experimentally investigated at the University of Maryland by Lee et al. [7]. The flowfield data was obtained by 2D PIV, while the rotor performance was measured by a micro mass balance. Once the CFD analysis was complete, the flows produced were used for safety analyses in terms of forces produced on ground personnel, properly scaled, using the PAXman model, and the presence of particles. To obtain realistic full-scale scenarios, a scaling factor has been applied to velocities using three different aircraft, categorized in terms of weight. After this, safe zones are defined where it was possible to consider the outflow forces and the presence of the particles as negligible. Existing safety separation criteria can then be tested. A possible separation distance is suggested by FAA for wake encounters [9] [3]. In that case, a distance of 3 rotor diameters is suggested to allow for dissipation of the wake generated by a rotor in hover or taxiing. Investigations are conducted to verify if the same distance can be considered safe for forces due to the outflow acting on ground personnel and for the presence of particles in the area that can spoil the pilot view of a near aircraft or hit people operating inside the 3 rotor diameters area. All CFD simulations have been performed using the HMB3 (Helicopter Multi-Block) CFD solver of Glasgow University.

## 2. Numerical models

### 2.1 CFD solver

HMB3 (Helicopter Multi-Block) [10, 11] is the solver used for all CFD calculations in this work. It solves the Unsteady Reynolds Averaged Navier-Stokes equations (URANS) in integral form with ALE formulation (Arbitrary Lagrangian Eulerian) for time-dependent domains (moving boundaries). URANS equations are discretized using a cell-centred finite volume approach on a multiblock structured grid. HMB3 uses the Osher [12] and Roe [13] approximate Riemann solvers to evaluate the convective fluxes, the viscous terms are discretized using second order central differencing. Third order accuracy in space is provided by the Monotone Upstream Centred Schemes for Conservation Laws (MUSCL) [14]. To avoid non-physical spurious oscillations, HMB3 solves uses the alternative form of the Van Albada limiter [15] where large gradients are involved in computations, like in presence of shockwaves. An implicit dual time stepping method is employed to perform the temporal integration. Oversets grids (used in this work) [16] and sliding plane [17] methods are available in HMB3 to allow for the relative motion between mesh components, representing ground and rotor blade. Various turbulence models are available in HMB3, including one-equation, two-equation, three and four equations turbulent models. Large-eddy Simulation (LES), Detached-Eddy Simulation (DES) and Delay-Detached-Eddy Simulation (DDES) can also be used with HMB3. For this study two different turbulence model have been used:  $k - \omega$  and  $k - \omega$  SST [18]. Furthermore, due to the low Reynolds numbers of the test cases some laminar simulations were also performed.

## 2.2 Scaling Factors for Flowfield

Analysing flowfield velocities generated by small-scale rotors is not adequate for safety purposes. Their speeds are simply too low. For this reason, scaling factors have been applied to the flowfield velocities. Small-scale refers to the micro-rotors operating conditions as presented in the experimental paper, listed in Table 1. A first scaling is necessary to obtain values comparable to full-scale rotor wake velocities. The blade tip velocity has been used, as listed in table 2 for full-scale rotors. However, a second scaling is necessary to take into account the difference in  $C_T$  of the different categories of helicopters. A common reference value for outflow velocities is the hover induced velocity, scaled with  $V_{tip}$ ,  $\lambda_i$ , expressed as  $\lambda_i = \sqrt{C_T}/2$ . The small scaled rotor thrust coefficient obtained by the simulation of the micro rotor is about  $C_T^{ss} = 0.03$ , while the  $C_T^{fs}$  can be obtained by the data, considering the aircraft in hover flight, and different disk loading categories.  $DL$ ,  $V_{tip}$ , and  $S_{rotor}$  are specified in table 2, while  $\rho_{air} = 1.225 \text{ kg/m}^3$  is assumed. Thrust and torque coefficients are presented in UK convention. It is possible, taking into account the effect of the different thrust coefficient to scale the velocities using the ratio of hover induced velocity between full-scale and small-scale cases. The scaling factor obtained is  $\sqrt{\frac{C_T^{fs}}{C_T^{ss}}}$ . This way, it is possible to approximate the outflow velocities generated by a full-scale rotor operating at the same high values of thrust coefficient of the scaled rotor. It is important to say that this kind of scaling cannot fully represent the complexity of the phenomena involved. This approach does not take into account the different Reynolds numbers that are involved in full and small scale rotors, that may significantly change the wake and its development in time.

$c$ (m)	$R$ (m)	$V_{tip}$ (m/s)	Re	$\theta_{75}$ (deg)
0.019	0.07	27	35000	12

**Table 1** Operational and geometric features of Lee et al. small scale rotor [7]

Category	Disk Loading ( $N/m^2$ )	$V_{tip}$ (m/s)	$C_T$
Light	280	220	0.0094
Medium	420	220	0.0141
Heavy	560	220	0.0189

**Table 2** Helicopters technical data [19]

## 2.3 PAXman model

The PAXman model was originally developed for military personnel, and it is used to compute wind forces on people operating in proximity to the rotor. It is based on the projection of a crouching 6ft tall person immersed in the outwash. The details of the geometry of the PAXman model are shown in Figure 1, as reported in [2] and [1]. To be comparable with the small rotor size, the PAXman height is scaled with the rotor radius for three different full-scale rotors, chosen to represent three different weight categories: light, medium and heavy. Their technical data are listed in table 2. The PAXman height has been scaled with the rotor radius, giving of  $h_{PAXman} = 0.3$  for the lighter aircraft, while for the medium and the heavy cases the result is the same, due to the similar size of the rotor radius, which lead to  $h_{PAXman} = 0.2R$ . Using the reference area expressed by the polynomial representation of Figure 1, the distribution of the force produced by the outwash on the ground personnel is computed as proposed in [2]. As mentioned early, to obtain comparable forces with the safety criteria, velocities are scaled using the blade tip velocity (table 2). On the other hand, the second scaling is necessary to take into account the difference in  $C_T$  of the three different cases, and for this reason the dimensionless hover induced velocity  $\lambda_i$ , expressed as  $\lambda_i = \sqrt{C_T}/2$ , has been used computed from Disk loading. According to [2] and [1] the caution zone starts when the force acting on the PAXman is more than 80 lbf (335 N), and the hazard zone is defined after 115 lbf (510 N). The distribution of the force over the body is calculated as:  $f_{paxman} = \frac{1}{2} \rho_{air} V_{rad}^2 x$  where  $\rho_{air}$  is density of the air,  $V_{rad}$  is the radial velocity and  $x$  is the horizontal coordinate of the PAXman model. The total force is the integral of the distribution of the force over the height of the PAXman

model.

$$F_{paxman} = \int_{h_{PAXman}} f_{paxman} dz \quad (1)$$

Using this model it is possible to calculate the force distribution acting on a human body at a specific radial station.

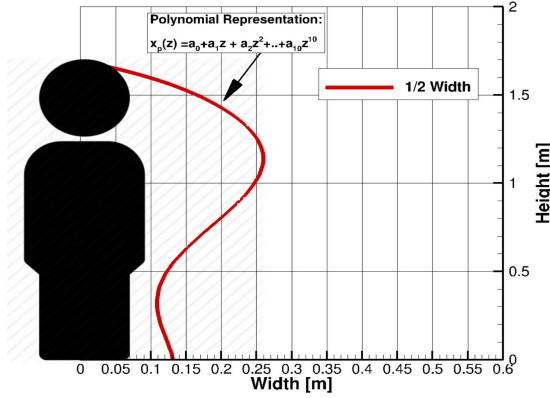


Fig. 1 PAXman model [1]

a0	4.31e-01
a1	-4.64e-02
a2	-1.40e-01
a3	1.37e-01
a4	1.37e-01
a5	-5.50e-04
a6	2.22e-04
a7	-4.18e-05
a8	1.45e-05
a9	-7.80e-08
a10	-1.90e-07

Table 3 Polynomial coefficients used in Figure 1

## 2.4 Particle tracking

Brownout and whiteout are due to the presence in the flowfield of particles. The former involves sand, and the latter snow. However, other kinds of particles can be involved such as rain, ice and even small rocks. There are basically two approaches for the numerical simulation of dispersed phases, and they can be categorized as Lagrangian and Eulerian. In the Lagrangian approach, the particles (or parcels of particles) are tracked through the field and the local cloud properties are defined by their properties as they pass a point in the field. For methods that involve this approach the motion of the particles is tracked using Newton's second law. Previous works in Lagrangian frame of reference are [20] [21]. For Eulerian methods, the properties of the particles are assumed continuous within the field. Thus, differential conservation equations are written and discretized, and the solution of these gives the properties of the cloud [22], [23]. A particle tracking tool has been developed for this work. It includes a pick up model, based on threshold velocity, a bombardment model and the effective tracking of particle using a Lagrangian frame of reference.

### 2.4.1 Threshold model

When the wake reaches the ground and interacts with the loose sediment, particles can be uplifted. To simulate this phenomenon, the Bangold model (see [24, 25]) has been used in several works. The Bangold model has been developed within the sediment research community to simulate the pick up of particles in river flows. In 2000 Shao et al. [26] proposed a formulation, based on the Bangold model, that has been adopted in this work. It is a threshold model, based on the wall friction velocity  $u_* = \sqrt{\frac{\tau_w}{\rho}}$ . The threshold value depends on particle and fluid properties and on the gravity. It is computed as:

$$u_t^* = \sqrt{A \left( \frac{\rho_p}{\rho_{air}} g d_p + \frac{\beta}{\rho_{air} d_p} \right)}, \quad (2)$$

where  $u_t^*$  is the threshold velocity, while  $A$  and  $\beta$  are coefficients:  $A=0.0123$ ,  $\beta=0.0003 \frac{kg}{s^2}$ . The particle properties, used in this work, are listed in Table 4, while for air and gravity the following values have been used:  $\rho_{air} = 1.225 kg/m^3$  and  $g = 9.81 m/s^2$ . When  $u^* > u_t^*$  particles are uplifted and entrained the flowfield.

$\rho_p$ ( $kg/m^3$ )	$d_p$ ( $\mu m$ )	$C_D$	$B$ ( $kg/m^2$ )	$u_t^*$ ( $m/s$ )
2650	9	1.048	0.03	0.58

**Table 4** Properties of particles used in this work.

#### 2.4.2 Splash Entrainment

When an entrained particle hits the ground, it may have sufficiently high energy to launch more particles. The kinetic energy gained by the hit particles can overcome the cohesive forces and lead to uplift. Once the particle hits the ground, it rebounds and enters again the flowfield. This phenomenon is called splash entrainment, and in this work, it has been modelled using a probabilistic approach, proposed in [27] and [28]. Before describing how the splash entrainment works, it is necessary to model the particle wall interaction using the hard sphere model, which is described in [29]. It is based on the integrated form of the equations of motion, and instantaneous deformations of the particles do not appear in the formulation explicitly. Considering the difference of the momentum between two generic time-steps (a and b). The momentum difference is equal to the impulsive force acting on the particle during that time period.

$$\mathbf{J}^{(b)} = m(\mathbf{u}_p^{(b)} - \mathbf{u}_p^{(a)}) \quad (3)$$

Computing the impulsive force acting before and after the collision, it is possible to compute the post-collisional translation velocities, solving the momentum equations. The hard sphere model introduces the following assumptions: 1) Particle deformations is neglected, and during the collision process, the particle radii are constant. 2) Coulomb's friction law applies to particles that are sliding along a wall. Considering three different timesteps:  $t=0$  pre-collision time,  $t=1$  collision time and  $t=2$  post collision time, as described in Figure 2. We can define two different impulses acting on the particles during impact:

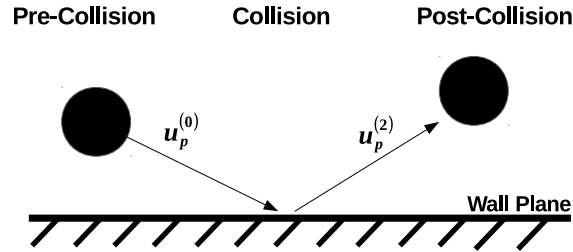


**Fig. 2** Schematic representation of particle-wall interaction

$$\mathbf{J}^{(1)} = m(\mathbf{u}_p^{(1)} - \mathbf{u}_p^{(0)}), \quad (4a)$$

$$\mathbf{J}^{(2)} = m(\mathbf{u}_p^{(2)} - \mathbf{u}_p^{(1)}). \quad (4b)$$

Considering a 3D case, with mass-point particles, and the wall perpendicular to the Z axis. It is possible to define a boundary condition at the wall as:

$$u_{pZ}^{(1)} = 0. \quad (5)$$

In [29] the definition of the coefficient of restitution  $e$  is given by:

$$J_Z^{(2)} = eJ_Z^{(1)}. \quad (6)$$

In this work  $e = 0.6$ , this coefficient represents the loss of momentum due to inelastic effects. From Coulomb's friction law, we have:

$$J_X^{(1)} \mathbf{i} + J_Y^{(1)} \mathbf{j} = -\varepsilon_X f J_Z^{(1)} \mathbf{i} - \varepsilon_Y f J_Z^{(1)} \mathbf{j}, \quad (7a)$$

$$J_X^{(2)} \mathbf{i} + J_Y^{(2)} \mathbf{j} = -\varepsilon_X f J_Z^{(2)} \mathbf{i} - \varepsilon_Y f J_Z^{(2)} \mathbf{j}. \quad (7b)$$

Here,  $f$  is the coefficient of kinetic friction ( $f = 0.2$  in this work),  $\varepsilon_X$  and  $\varepsilon_Y$  are factors indicating the proportion of the velocity in each wall plane component direction, and are defined as

$$\varepsilon_X = \frac{u_{pX}}{\sqrt{u_{pX}^2 + u_{pY}^2}}, \quad \varepsilon_Y = \frac{u_{pY}}{\sqrt{u_{pX}^2 + u_{pY}^2}}. \quad (8)$$

From this definition, it is possible to see that  $\varepsilon_X^2 + \varepsilon_Y^2 = 1$ . In this work, these values are constant during the collision processing, in other words:  $\varepsilon_X^{(0)} = \varepsilon_X^{(1)} = \varepsilon_X^{(2)}$ , and the same for  $\varepsilon_Y$ . Considering the velocity of the impacting particle, the friction and restitution coefficients it is possible to solve the system for the 12 unknowns (three components of velocity and three components of the impulse force acting on a particle at times (1) and (2)). The rebound velocity components of the particles are:

$$u_{Rx} = u_{px}^{(0)} + \varepsilon_X f (1 + e) u_{pz}^{(0)}, \quad (9a)$$

$$u_{Ry} = u_{py}^{(0)} + \varepsilon_Y f (1 + e) u_{pz}^{(0)}, \quad (9b)$$

$$u_{Rz} = -e u_{pz}^{(0)}. \quad (9c)$$

In the case of no emitted particles during the impact ( $N_s = 0$ ), the rebound velocity is the velocity of the particle rebound, in other words  $\mathbf{u}_R(N_s = 0) = \mathbf{u}_p$ . However, if other particles are emitted, the kinetic energy, due to the rebound velocity, is shared among all emitted particles. After computing  $N_s$ , using the momentum and energy conservation law it is possible to compute the average and standard deviation of particles velocity.

### 2.4.3 Particle motion equation

For particle tracking, an in-house simulation method has been used. The particles are driven by the flowfield velocities and their positions in time are obtained by integrating their equations of motion. The integration method used is a fourth order Runge-Kutta, and the equation for particle tracking acceleration is:

$$\mathbf{a}_p = \frac{0.5 \rho_{air} (\mathbf{u} - \mathbf{u}_p) \|\mathbf{u} - \mathbf{u}_p\|}{B} - \mathbf{g}, \quad (10)$$

where  $\mathbf{a}_p$  is the acceleration of the particle,  $\mathbf{u}_p$  is its velocity,  $\mathbf{u}$  is the velocity of the flowfield in the position of the particle and  $B$  the particles ballistic coefficient,  $B = \frac{m_p}{S_p C_D}$ . Here  $m_p$  is the particle mass,  $S_p = \pi d_p^2 / 4$  is the particle frontal area (particles are assumed spherical),  $C_D$  is the particle drag coefficient, and finally  $\mathbf{g}$  is the acceleration of gravity. The particle properties used in this work are listed in table 4, they reflect the size and the density of particles used to simulate brownout in experimental and computational works [27] [28] [30]. The particle motion equation has been non-dimensionalized using the flowfield reference values for length, velocity and density. The reference value  $l_{ref} = c$  is the rotor blade chord,  $V_{ref} = V_{tip}$  the rotor blade tip velocity and finally  $\rho_{ref} = 1.225 \text{ kg/m}^3$ . As integration method to solve the particle acceleration equation, a fourth order Runge-Kutta has been used. To obtain the velocity and position of particle at any timestep, it is necessary to integrate two vector equations, one to obtain the particle velocity, one for the position:

$$\begin{aligned} \frac{\partial \mathbf{u}_p}{\partial t} &= \mathbf{a}_p(t_n, \mathbf{u}_p^n), \\ \frac{\partial \mathbf{x}_p}{\partial t} &= \mathbf{u}_p(t_n, \mathbf{x}_p^n). \end{aligned} \quad (11)$$

#### 2.4.4 Search algorithm

During the entire particle tracking process it is necessary to know the velocity and density values of flowfield in the space occupied by the particle. In other words, the particles have to be located inside the computational domain. To do this, a search method has been developed. When the flowfield is seeded with particles in the first time step, the distance between the particle starting position and the centre of all the grid cells is computed. The seeding particle is then assigned to the nearest cell in the domain. This "brute force" searching method is expensive in terms of computational cost, and it is done only during the first time step to have starting particle positions inside the computational domain. However, after the first time step it is possible to adopt a faster search, using the particle initial position as starting information. To avoid an extremely high computational cost, the searching area is delimited around the neighbour cells of the particle position at the  $t_n$ . The searching method is described in Figure 3, the search area (the darkest area in the Figure) is delimited by the maximum distance travelled by the particle during the  $\Delta t$  between time instances  $t_n$  and  $t_{n+1}$ . The area is delimited by the maximum range,  $r_{max}$ , computed as:  $r_{max} = \mathbf{u}_p \Delta t$ . The  $i$ -th cell is considered in the search area if  $r_i < r_{max}$ , where  $r_i$  is the distance between the  $i$ -th cell centre  $x_i$  and the position of the particle at  $t_n$ ,  $r_i = \|\mathbf{x}_p^n - \mathbf{x}_i\|$ . The particle is then searched in the delimited area, comparing the distance between the cell centre and the particle position at  $t_{n+1}$ , finally the particle is assigned to the nearest cell. Once a particle is found, an interpolation is done to compute the flowfield properties in the space occupied by the particle. All cells around the particles are taken into account for this, the influence of all the cells is weighted with respect to the distance. In all simulations the grids were hexaedrical, so the cells around the particles plus the one that contains the particle, are 27 in total, in far from a boundary condition. According to this:

$$u_{flow}(x_p^{n+1}) = \sum_{i=0}^{27} \frac{u_{flow}(x_i)}{q_i}, \quad (12a)$$

$$d_i = \|\mathbf{x}_i - \mathbf{x}_p^{n+1}\|, \quad (12b)$$

$$q_i = \frac{d_i}{\sum_{i=0}^{27} d_i}. \quad (12c)$$

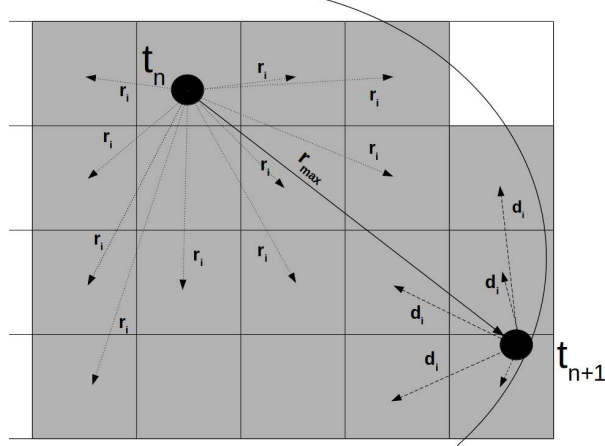


**Fig. 3 Search algorithm for particle tracking**

In the above,  $u_{flow}(x_p^{n+1})$  is the flowfield velocity in the position occupied by the particle and  $u_{flow}(x_i)$  the flow velocity in the centre of the  $i$ -th cell.  $x_i$  is the position of the  $i$ -cell centre, while  $x_p^{n+1}$  is the particle position at timestep  $n+1$ . When the code runs in parallel every particle is associated to a single processor, which search in the flowfield only its particles, ignoring the others.

#### 2.4.5 Parallel particle tracking

The particle tracking code has been developed to run in serial and in parallel. When the code runs in parallel, the total amount of particles is divided among the processors. In this way, every particle is associated to a processor, which tracks it for the whole simulation. First, the method reads the mesh and the input file, which contains information about the particle properties (density, radius, drag coefficient), seeding particle starting position, flowfield information (Reynolds number) and gravity. Then, it reads the flowfield files, and releases the particles in the flowfield. When a new particle is released in the flowfield, it is assigned to a single processor. Processors do not exchange information about particles, they track their particles from the first timestep to the end of the simulation. After generating particles, every processor searches and updates the position of every particle that is associated to it. The searching and updating schemes have been described previously. Finally, each processor writes an output file containing all the particle position at the timestep, which are later postprocessed in a single file. The flow chart of the algorithm is presented in Figure 4.

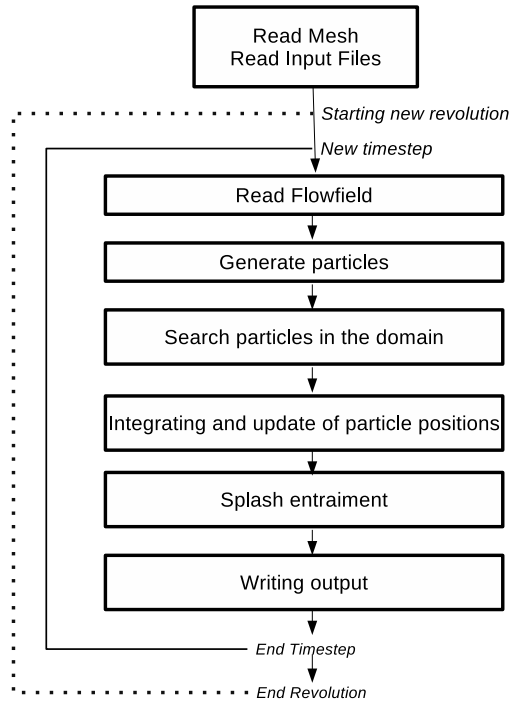


**Fig. 4 Particle tracking flow chart**

The total execution time is shown in Fig 5 (a) for 10 revolutions, using a different number of seeding particles, and different number of processors. Results show, as expected, a linear behaviour. The execution time increase with the number of seeding particles tracked, however the linear slope is slower considering the number of processors used. All processor tracks the same number of particles, improving the performance linearly with the number of processors used. A coarser mesh has been used for these results (1.6 M). In Figure 5 (b) the speed up of the total execution time is compared with the ideal linear behaviour. In an ideal parallel strategy, the speedup of a process runned in parallel grows linearly with the number of processors. Results show that the particle tracking timing is closer to the ideal case when a smaller amount of processors is used, this is in accordance with the Amdahal's law. [31]. In Fig 5 (b) it is also possible to compare the speed up of different tests, with different number of seeding particles. When the amount of particles is larger, the timing behaviour is slightly closer to the ideal case with respect to the case with a lower amount of seeding particles. Considering a fixed number of revolutions, the serial part of the code does not change with the amount of particles, on the other hand the parallel part increases with it, resulting in better performances with a bigger number of processors used.

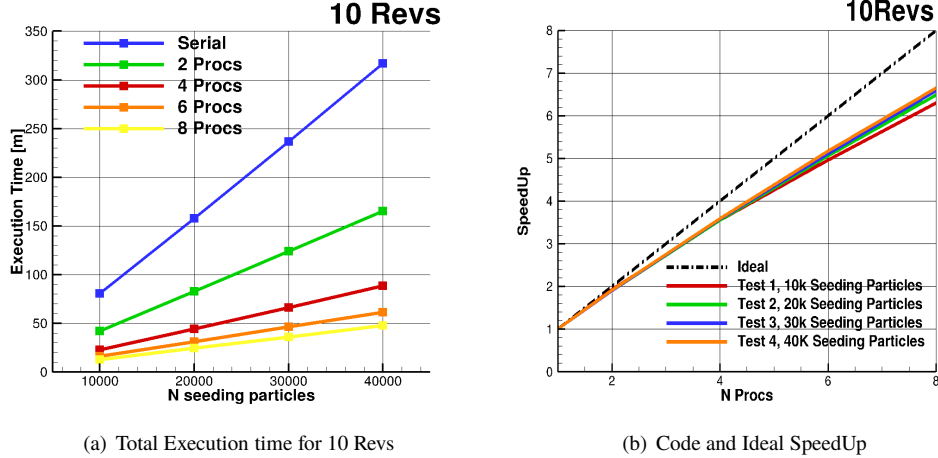
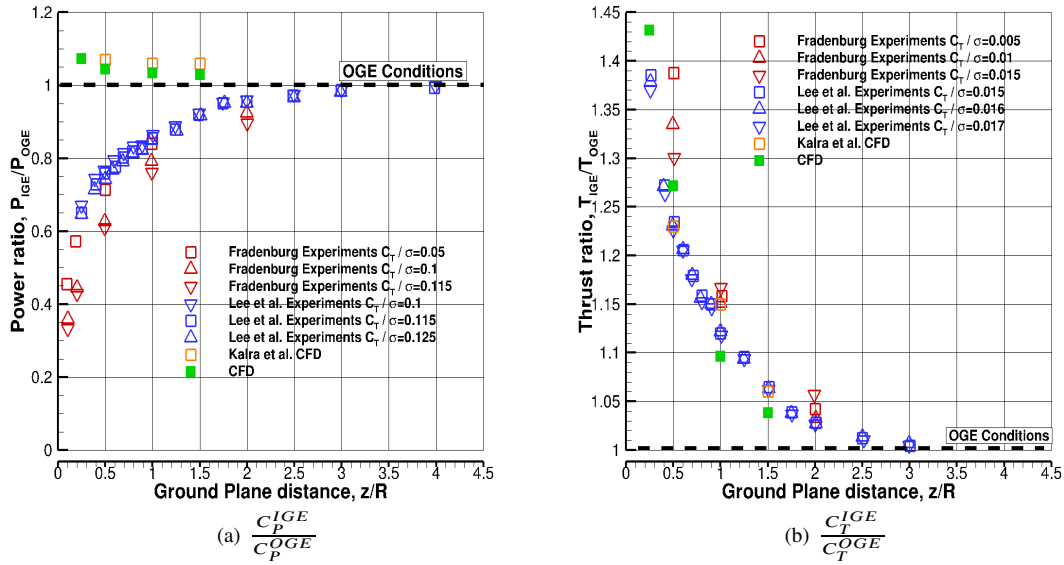


Fig. 5 Total time for particle tracking

### 3. Computations and Safety Considerations

#### 3.1 CFD Validation - Rotor performance and Outflows

Previous works showed the full validation of the same test case in OGE [32]. The IGE the rotor was modelled using two overset grids, and the ground was modelled imposing no-slip conditions. The full rotor domain was computed as unsteady. The unsteady time step was changed during the simulation. The first two revolutions were computed at 5deg/timestep. Then, the timestep was gradually reduced reaching 0.5deg/timestep for the last revolutions performed. In total 5 full revolutions were simulated. The mesh has been refined near the ground and the rotor to accurately resolve the wake features. Three different rotor heights above the ground configuration were tested:  $h/R=0.5$ ,  $h/R=1$  and  $h/R=1.5$ , all of them with collective  $\theta = 12deg$ . Comparisons in terms of performance are given in Figure 6 ( $C_T^{IGE}/C_T^{OGE}$  and  $C_Q^{IGE}/C_Q^{OGE}$  ratios) and show small differences with the experiments of [7]. The thrust coefficient shows results very close to the measurements by Lee et al. [7] for all three rotor heights. The increment of thrust coefficient IGE is about 4% for 1.5 radius height, 12% for  $h/R=1$  and finally 28% for 0.5R with respect to the OGE case. In general, these results agree with experimental data, in particular the error between experiment and CFD results in terms of  $C_T^{IGE}/C_T^{OGE}$  is about 3% with  $h/R=0.5$ , 2% for  $h/R=1$ , and for  $h/R=1.5$  the error is 3%. The results in terms of the power coefficient are very similar for all cases, and they are slightly higher than expected. However, it can be considered that the power between OGE and IGE is fairly constant for all the rotor height configuration, with a small increment in the thrust coefficient, as expected. Similar results in terms of  $C_Q^{IGE}/C_Q^{OGE}$  have been obtained by Karla et al. in [33] for the same test case. In Figure 7, the rotor wake is presented as (a) iso-surfaces of Q-criterion and (b) contours of vorticity magnitude, for  $z/R=1$  configuration. The Q criterion is related to the velocity gradient tensor, and its iso-surfaces are a good indicator of how vortical flow may be [34]. It is possible to notice how the wake initially contract inside the rotor area, and then expand as the tip vortices reach the ground. Contour levels in Fig 7 (b) show how the vorticity contained in the vortices diffuse. The higher vortex is smaller and with high vorticity values with respect to the vortices in proximity of the ground. Finally, it is also noticeable the presence of the starting vortex in proximity of 1.2R. Its strong influence on the seeded ground will be discussed in later sections.



**Fig. 6** Experimental and CFD results for the power and thrust ratios IGE. The rotor was operating at  $\theta_{75} = 12deg$ ,  $Re_{tip} = 35000$  and  $M_{tip} = 0.08$ . Experimental data taken from [7] and additional CFD data from [33].

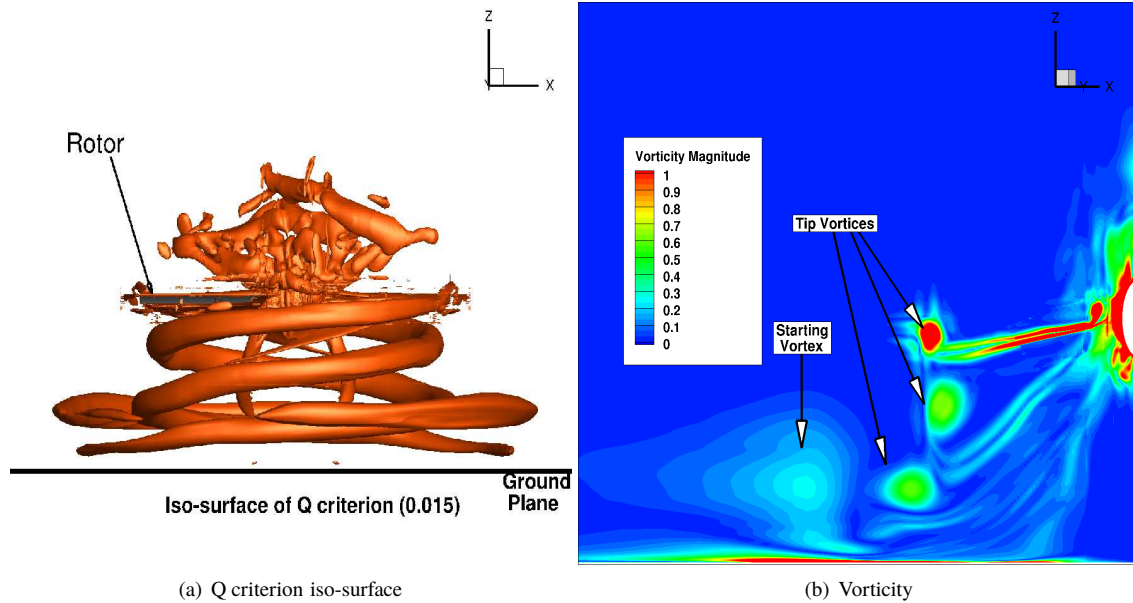


**Fig. 7** Wake Visualization, for the IGE case. The rotor operating at  $h/R=1$ ,  $\theta_{75} = 12deg$ ,  $Re_{tip} = 35000$ ,  $M_{tip} = 0.08$ ,  $h/R = 1$  and  $C_T = 0.03$ .

In Figure 8 the time-averaged radial velocities are shown in comparison with experiments for the three different cases. The time-averaged outflow has been scaled using two different velocities. The left columns of Figures 8 show results scaled with the reference hover induced velocity  $v_i = \frac{\sqrt{C_T}}{2}$  (as proposed by Lee et al. [7]), while on the right column the same results are scaled as a jet, using the peak radial velocity  $v_{max}$ . Finally, the dashed line represents the PAXman model height for the heaviest helicopter size.

At a radial distance of  $r/R=1$ , the radial velocity peak is reached around  $0.2R$ , independently to the rotor distance from the ground, with a scaled maximum velocity around 1.5 for all three rotor configurations. For this radial station, the momentum is well distributed along the distance between the rotor and the ground in the case of rotor at  $h/R=0.5$  and  $h/R=1.0$ , while for the case at  $h/R=1.5$  the momentum is more localized in the proximity to the ground. On the other hand, for  $r/R=2$  the momentum is concentrated in proximity of the ground for all three rotor configurations, with a lower peak position. In this case, the oscillations, due to the rotor proximity, are almost dissipated and the outflow is well established, defining the jet like flow of rotors IGE. In general, the time-averaged velocities show good agreement with experiments in terms of maximum radial velocity and outflow distribution for both scaling methods at lower radial positions in all three rotor configuration. For the radial position at  $r/R=1$ , with  $h/R=0.5$ , the error at the peak is around 13% (overestimated), 20% for  $h/R=1$  (underestimated) and almost negligible for  $h/R=1.5$ .

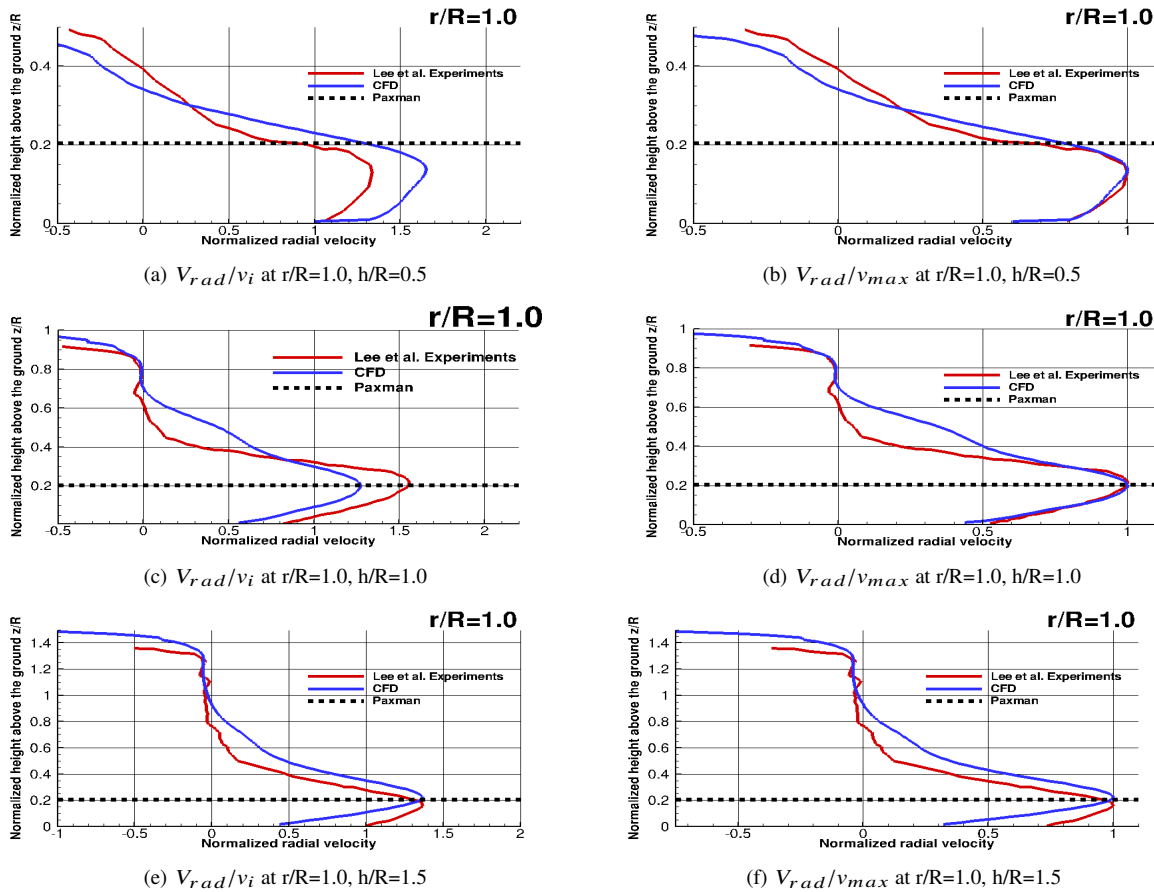


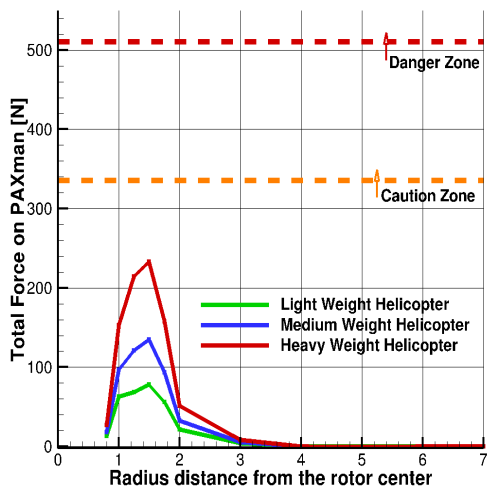
**Fig. 8** Experimental and CFD time-averaged outflow velocity profiles at different radial positions. The rotor was operating,  $\theta_{75} = 12deg$ ,  $Re_{tip} = 35000$ ,  $M_{tip} = 0.08$  and  $C_T = 0.028$ . Left column results are scaled with induced hover velocity, while the right column results are scaled with jet-scaled velocity. Experimental data taken from [7].

### 3.2 PAXman results

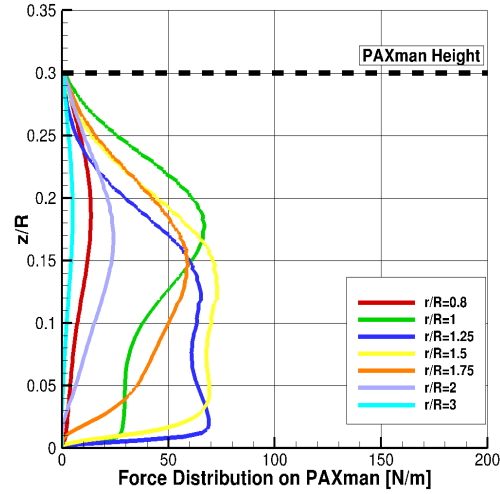
Figures 9 (a), 10 (a) and 11 (a) show the total forces acting on a scaled human body at different distances by the outflow produced by the rotor for the three different rotor configurations. As mentioned before, the forces have been computed scaling the velocities with the  $V_{tip}$  of full-scale aircraft, to obtain more realistic values and compare them with the safety thresholds suggested for civilian and military operations. The forces for all three rotor configurations reach their peaks at a radial distance between 1.25R and 1.5R, but they weaken for larger radial stations. This result is due to the outflow distribution at different radial stations, with the higher velocities occurring around 1.5R. For all three rotor distance from the ground, the strongest force is produced by the aircraft with higher  $C_T$ , which is the heaviest helicopter taken into account. In general all results are lower with respect to the caution limit of PAXman model. When the rotor is operating at  $h/R=1.5$  and  $h/R=1$ , the forces reach similar peaks, around 270 N, for the heavy weight helicopter, slightly stronger than the configuration at  $h/R=0.5$  for the same weight aircraft category. In all cases, after 2R, the forces drop quickly. This is due to the outflow velocities that drops away from the rotor. After 3R the forces are almost negligible based on the PAXman model for all three scaling factors and for all three rotor distances from the ground. Figure 9 (b), (c) and (d) show the distributions of the forces over the PAXman height at different radial stations for the three helicopters. For all three cases, near the rotor the force is strongest at a specific PAXman height (corresponding to the PAXman chest). This result is due to the shape of the outwash distribution and the larger blocking area at the chest level. This result is in accordance with other experiments. In [2] the force peaks were around the middle of the human body, however the experiments performed by Silva et al, were full-scale. Figure 9 (b) shows the results for the light aircraft. Here the PAXman height is higher with respect to the other two cases. This is due to the smaller size of the rotor blade of the lightest helicopter. This leads to a difference in the force distribution for the light helicopter with respect to the heavier cases. For all three rotor distance from the ground, the lighter helicopter results show a force distribution well distributed over the PAXman body, with a minor stress over the chest area. On the other hand, the medium and heavy cases show a stronger stress for this part of the body. In general, the forces for lighter helicopter at every radial distance are smaller with respect to heavier cases. This is in agreement with what is shown in Figure 9 (a), where the lightest aircraft produces weaker forces in comparison to the medium and the heavy. PAXman forces distributions for  $h/R=1$  and  $h/R=1.5$  are shown in Figures 10 (b), (c), (d) and 11 (b), (c), (d). Similar to  $h/R=0.5$ , the most exposed part of PAXman body is the chest, with the strongest forces at a radial distance about  $r/R=1.5$ . In general, heavier helicopter outflows are stronger with respect to the light cases, and the PAXman chest area is the most exposed to stress due to strong forces.

### 3.3 Uplift and Particle tracking

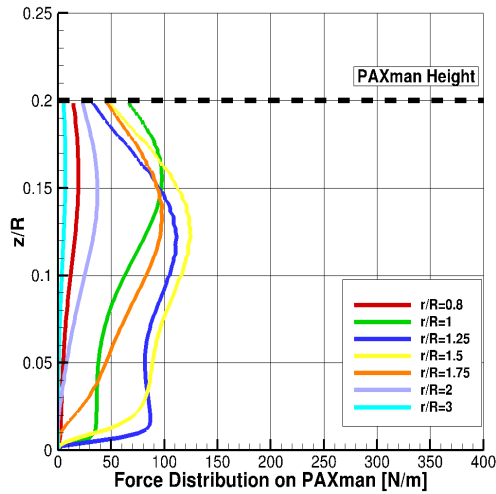
Figure 12 shows results for the threshold model. Using the computed shear stress on the ground of the domain, it was possible to calculate directly friction velocity, and using, the Bangold threshold model, the particle uplift locations. In general, results show that the peak of the uplift ratio  $u_t/u_t^*$  is in proximity of 1 R distance from the rotor, and the area of uplift particles for the cases considered is at least between 1R and 2R. This is due to the presence of the starting vortex in proximity of the ground shown in Fig 7. Heavier helicopters produce stronger outflow, which may extend the uplift area up to 3R for  $h/R=0.5$ . The rotor distance from the ground has a key role in defining the area where particles may be uplifted. Results show that when the rotor operates at  $h/R=0.5$ , the particles can be uplifted up to a 3 rotor radius distance for heavy helicopter case, while for higher rotor altitude the uplift area can be delimited by 2R. Furthermore, considering the lighter weight (left column), in the case of  $h/R=0.5$  and  $h/R=1$ , uplift ratio drops slowly, with values of uplift ratio around 0.5 after 3R, while for  $h/R=1.5$  after the maximum the uplift drops quickly after 2R, reaching small uplift values at 3R. This leads to the result that the distance of the rotor from the ground have an influence on the scaling effect. In the case of  $h/R=0.5$ , the uplift area for the lighter helicopter is 2R, while it grows to 3R for heavier aircraft case, on the other hand for the rotor at  $h/R=1.5$ , the uplift area increment with heavier scaling is not so effective. In general, the rotor height has a strong effect on particles uplift locations, the uplift area is bigger with the rotor closer to the ground, and as for PAXman results, the heavier helicopter produces the most dangerous scenarios, with bigger uplift areas. Using this information it was possible to seed the ground with the particles that are more likely to be affected by the flowfield. Figure 13 shows the evolution of the particles with time for three weight helicopter cases taken into account, with the rotor at three different heights above the ground. Different seeding positions have been defined between 1R and 1.5R in proximity of the ground level. Bombardment effect has not been taken into account here. The simulations involve about 100 revolutions, for a total hover time of 30 seconds. The flowfield generated by the model rotor was not able to lift particles. As for the PAXman force computations, to obtain more realistic results



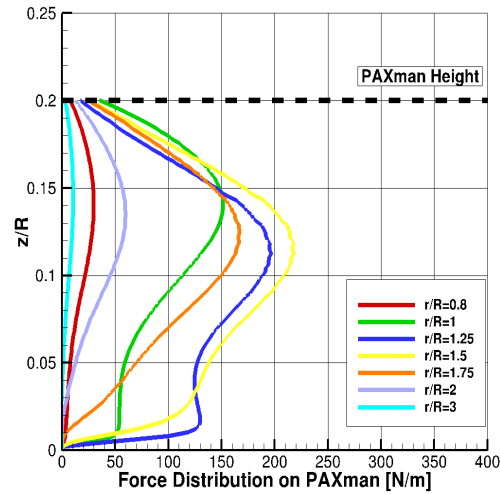
(a) Total radial force  $F_{PAXman}$  for the three helicopters



(b) Radial force distribution  $f_{PAXman}$  for light weight aircraft



(c) Total radial force  $F_{PAXman}$  for medium weight aircraft

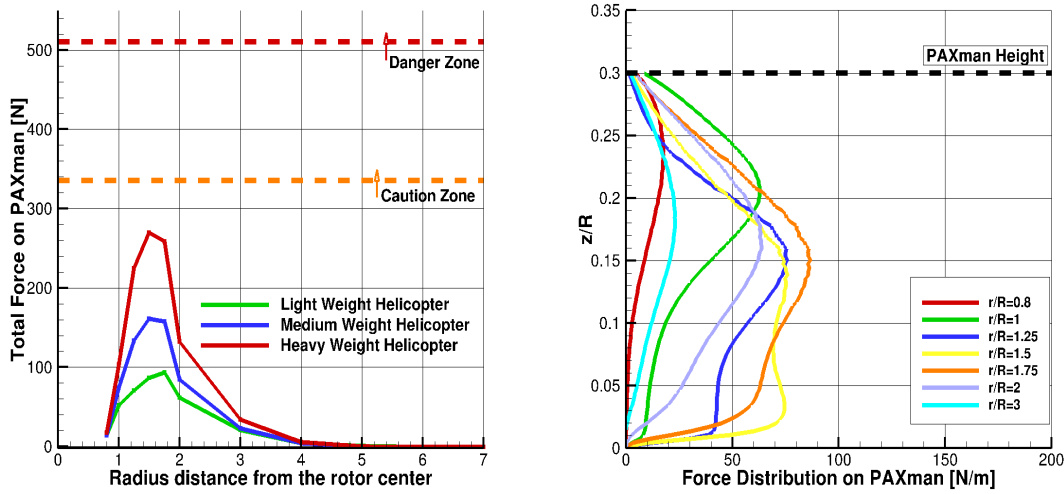


(d) Radial force distribution  $f_{PAXman}$  for heavy weight aircraft

**Fig. 9** PAXman model forces calculated using the employed micro-rotor, scaled to  $V_{tip}$  m/s. The micro rotor rotor was operating at  $\theta_{75} = 12deg$ ,  $Re_{tip} = 35000$ ,  $M_{tip} = 0.08$ ,  $h/R = 0.5$  and  $C_T = 0.035$ .

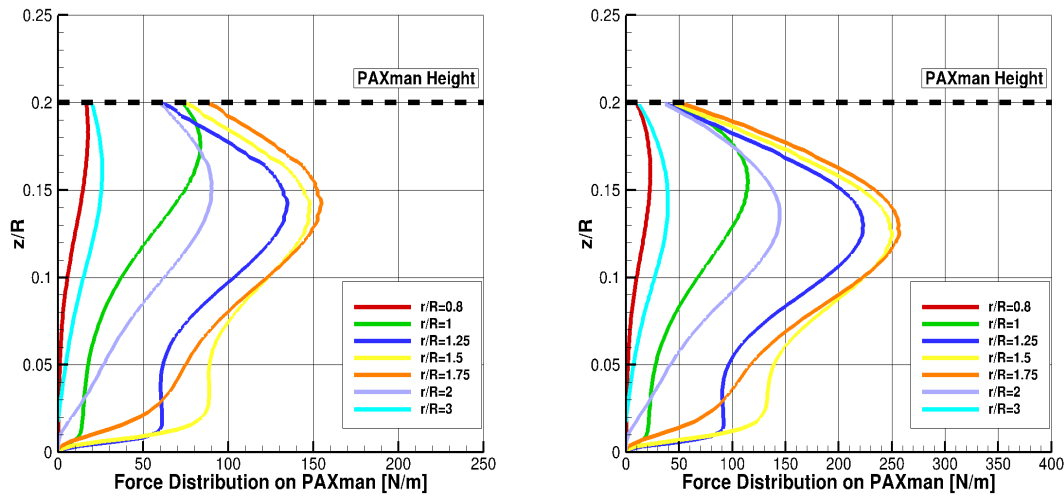
the flowfield has been scaled using a possible operational  $V_{tip}$  for light and heavy weight helicopters considered in table 2, and with the  $C_T$  scaling factor.

In Figure 13, the results are shown for particle tracking. Seeding points have been released in proximity of the ground, between 1 and 2R, as result of the uplift model. A new particle is released in the flowfield from the ground every 5deg. The full simulation involves 100 revolutions (about 30 seconds for a full scale rotorcraft). Due to the high computational cost of the CFD simulation, the last revolution performed has been considered periodic, and has been repeated for the full duration of the particle tracking. When the rotor is operating at  $h/R=1$ , the particles are uplifted by the flowfield, and then move away from the rotor, following the radial direction. Particles are driven by the outflow that pushes them away from the rotor. However, depending on the strength of the outflow they reach different positions.



(a) Total radial force  $F_{PAXman}$  for the three helicopters

(b) Radial force distribution  $f_{PAXman}$  for light weight aircraft

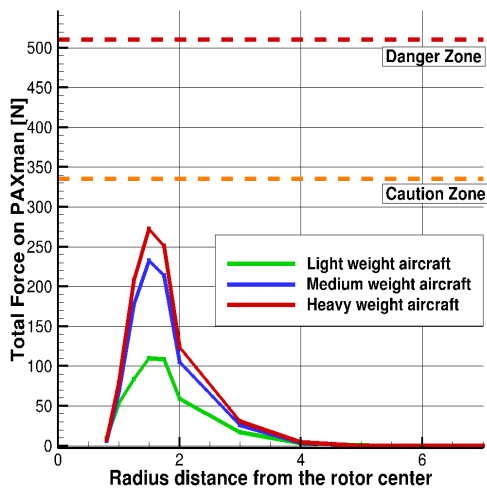


(c) Total radial force  $F_{PAXman}$  for medium weight aircraft

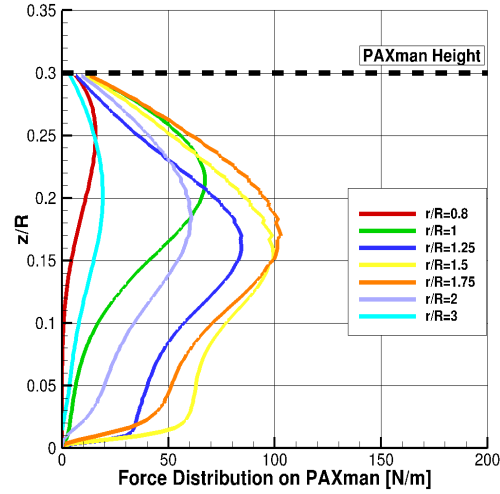
(d) Radial force distribution  $f_{PAXman}$  for heavy weight aircraft

**Fig. 10** PAXman model forces calculated using the employed micro-rotor, scaled to  $V_{tip}$  m/s. The micro rotor rotor was operating at  $\theta_{75} = 12deg$ ,  $Re_{tip} = 35000$ ,  $M_{tip} = 0.08$ ,  $h/R = 1$  and  $C_T = 0.03$ .

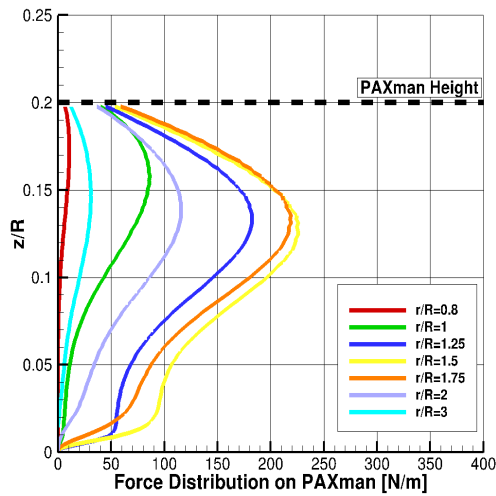
Heavy weight helicopters have a stronger outflow, and in this case, particles can reach a maximum radial distance of  $8.5R$ , and a maximum height above the ground of  $1R$ . Once the particles reach the maximum altitude value, they fall again on the ground. Lighter weight helicopter cases, show lower values for maximum  $h/R$  and  $r/R$ . However, particles go further the 3D separation criteria for wake encounters. In this case, the scaling have a minimum effect of particles paths increasing the maximum distance reached of about  $1R$  between light and heavy helicopter, with a very limited influence on the maximum height reached by particles. A similar path is followed in the case of  $h/R=1.5$ , where the particles reach a maximum height of  $h/R=1.5$  for the heavy weight aircraft case. As for the previous case, the maximum height is reached at  $r/R=6$ , however the flowfield seems weaker with respect to the previous case, particles reach a maximum radial distance of  $8R$ , in the most dangerous scenario. On the other hand, when the helicopter is operating at  $h/R=0.5$  particles show a different behaviour. Initially, particles are uplifted from the ground, then two main branches spread, following different paths. Some of them, are reingested by the rotor, reaching the highest distance from the



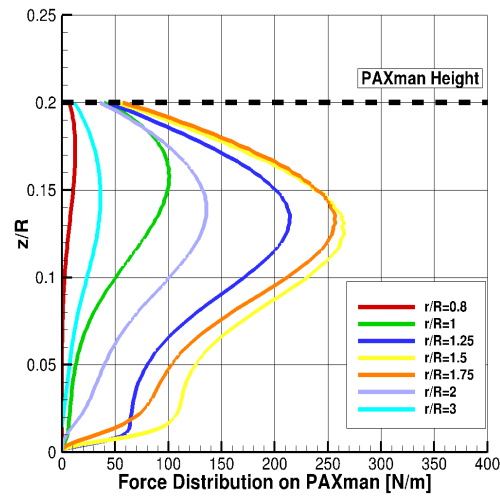
(a) Total radial force  $F_{PAXman}$  for the three helicopters



(b) Radial force distribution  $f_{PAXman}$  for light weight aircraft



(c) Total radial force  $F_{PAXman}$  for medium weight aircraft



(d) Radial force distribution  $f_{PAXman}$  for heavy weight aircraft

**Fig. 11** PAXman model forces calculated using the employed micro-rotor, scaled to  $V_{tip}$  m/s. The micro rotor rotor was operating at  $\theta_{75} = 12deg$ ,  $Re_{tip} = 35000$ ,  $M_{tip} = 0.08$ ,  $h/R = 1.5$  and  $C_T = 0.028$ .

ground. These particles can be dangerous for the crew and the aircraft. The rest of the particles keep following the radial direction far from the rotor, and fall again on the ground at distance around  $6.5R$  for the heavy scale helicopter. Like in the case of uplift results, the rotor position above the ground have a strong influence on particle path, defining the maximum height and distances reached by the particles, and whether particles are reingested or not. Scaling factors also have a role in defining the "safe zone" operation, heavier helicopter pushes farer away particles, increasing the radial cloud dimension. In general, as expected, the heavier helicopter shows the most dangerous scenario in all rotor configurations. When the helicopter is operating at  $h/R=1$ , the particles do not have a strong effect on pilot visibility. Up to a distance of  $3-4R$ , the particles are near the ground, and the pilot may see clearly the ground, avoiding ground obstacles and structures. On the other hand, particles may have an effect on the visibility of another helicopter operating nearby, entering in its operational area. A similar scenario is presented at  $h/R=1.5$ , even if it is slightly worse than the previous. Here the particles stay close to the ground up to  $2/3R$ , and they reach higher positions. This

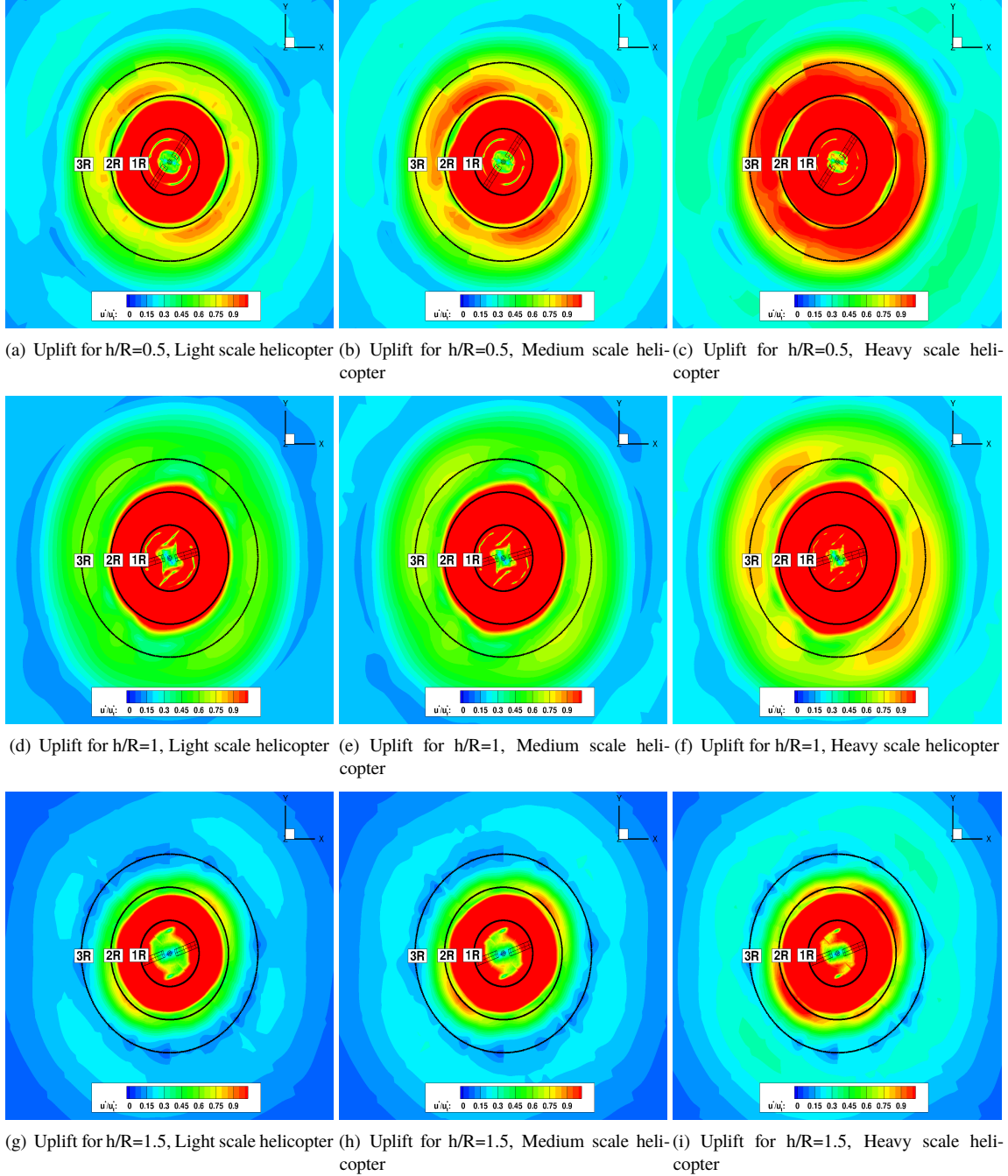


**Fig. 12 Uplift results for rotor at different heights above the ground and different scaling factors. The rotor was operating  $\theta_{75} = 12deg$ ,  $Re_{tip} = 35000$  and  $M_{tip} = 0.08$**

way, the pilot visibility is slightly reduced with respect to the  $h/R=1$  case. However, it may be still possible to see the ground in the rotor closer area. Finally, the most dangerous scenario, is with  $h/R=0.5$ . In this case, the pilot visibility is strongly reduced due to the particles reingestion, generating the dangerous DVE condition described in the introduction. Furthermore, during the re-ingesting phase particles can hit blades and fuselage, damaging rotor structures or being ingested by the engines. Particles that move away from the rotor can be dangerous for ground personnel, equipment and other aircrafts, while the recirculation of the particles creates risks for the helicopter and the crew itself due to the reingesting phase.

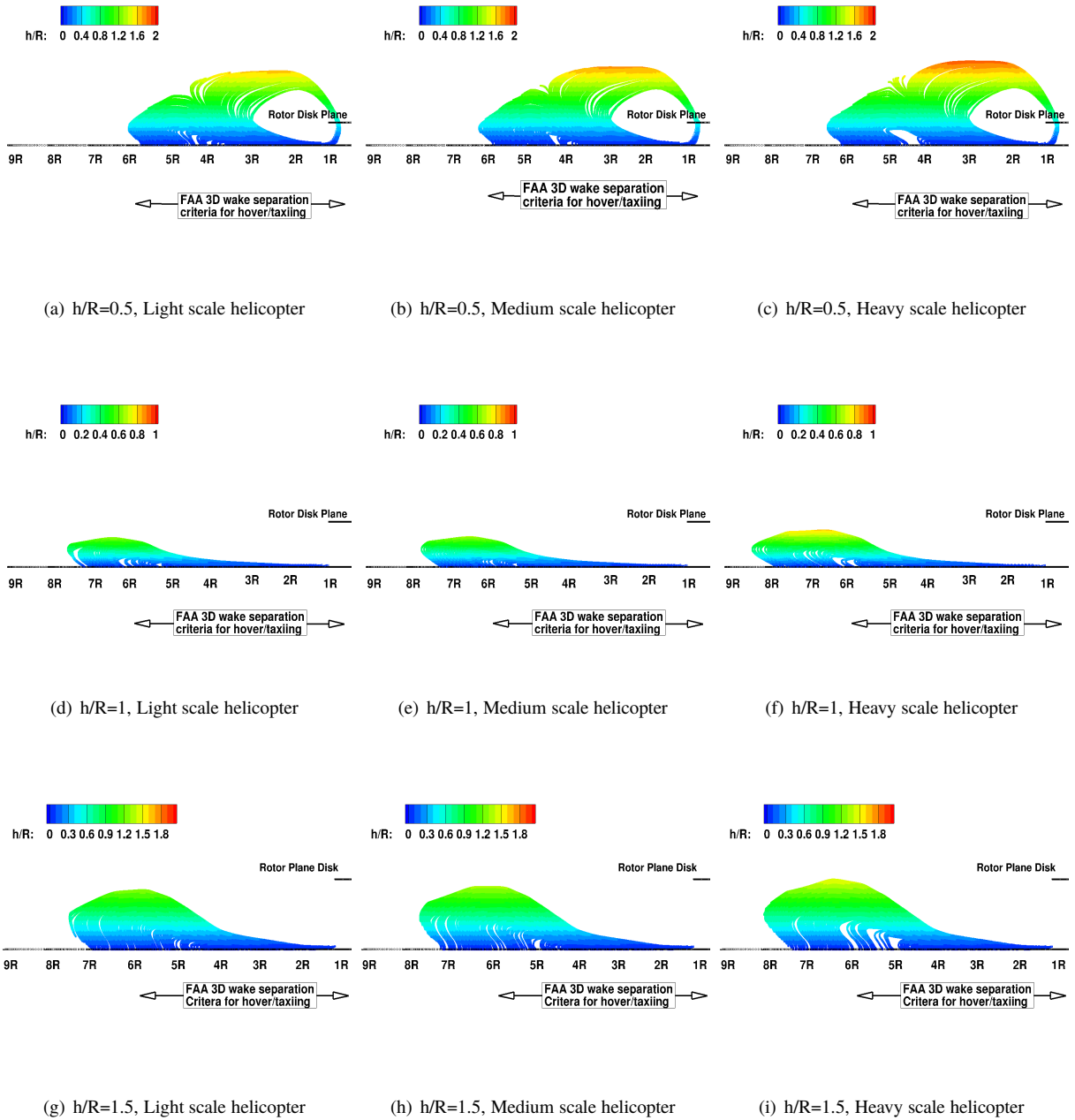


**Fig. 13 Particle paths for rotor at different heights above the ground and different scaling factors. The rotor was operating  $\theta_{75} = 12deg$ ,  $Re_{tip} = 35000$  and  $M_{tip} = 0.08$**

## 4. Conclusions and Future Steps

Safety considerations for full scale rotors have been studied starting from the analysis of a micro-rotor operating IGE at different heights above the ground.

Results show that the distance criterion based on the PAXman forces, can be deduced by the outflow analysis.

Outflow forces after a distance of 3R are low for the three helicopter cases considered. Furthermore, for the lightest helicopter, there is no risk due to the outflow forces for ground personnel. It is clear that the wake encounter criterion of 3D can be adopted for ground operation, if the presence of particles on the ground can be excluded. A more detailed analysis shows that the forces obtained for the medium and heavy aircraft are high enough to be dangerous for personnel and equipment in an area between 1R and 2R away from the rotor, but after 3R it is safer. The force distributions suggest that the chest is the part of the human body that is most influenced by the force due to the outflow, and this result can be part of the evaluation on definite safety regulations for people acting in proximity of the rotor. Particle tracking results show that particles can reach large distances away the rotor, exceed the limit of 3D. In general, it appears that the FAA limit for wake encounters cannot guarantee safety in presence of particles on the ground. It is also clear that to define a particle free zone, it is necessary to take into account the rotor operating conditions due to the strong influence of the disk loading and in general of the size of the aircraft on the particle paths. Particle paths are also strongly influenced by the position of the rotor with respect to the ground. The force distributions suggest that the chest is the part of the human body that is most influenced by the force due to the outflow, and this result can be part of the evaluation on definite safety regulations for people acting in proximity of the rotor.

CFD results demonstrate fairly good agreement with experimental data in terms of rotor performance and flowfield, even if there are some differences in the outflow predictions for radial stations far away from the rotor. The differences can be important if used to evaluate safety regions near the helicopter. Results employing different scaling approaches show different agreements with experiments, and only scaling with  $v_i$  gives a complete understanding of the outflow analysis in terms of safety. The normalized magnitude of the radial velocity peak in the outflow and its position, related to PAXman height, are fundamental to obtain correct force estimations.

In this work, scaling factors are applied to small-scale rotors to obtain full-scale PAXman forces and particle paths. However, the full physics of the brownout cannot be simulated in this way, due to the several factors. In general, the Reynolds number that is involved in the small and the full-scale scenario is dissimilar, leading to differences in the uplift phenomena and to a different evolution of the brownout cloud. This study can be a starting point for evaluating safe operational zones around a helicopter.

A future step will consist detailed simulations, to identify a proper safe zone from particles and compare it with other distance safety regulations like the 3 rotor diameters separation distance for wake encounters suggested in the Manual of Air Traffic Service [9] [3].

## Acknowledgments

This project has received funding from the European Union's H2020 research and innovation programme under the Marie Skłodowska-Curie grant agreement No 721920

Results were obtained using the EPSRC funded ARCHIE-WeSt High Performance Computer ([www.archie-west.ac.uk](http://www.archie-west.ac.uk)).

This work used the Cirrus UK National Tier-2 HPC Service at EPCC (<http://www.cirrus.ac.uk>).

This work used the ARCHER UK National Supercomputing Service (<http://www.archer.ac.uk>).

## Bibliography

- [1] Preston, J. R., Troutman, S., Keen, E., Silva, M., Whitman, N., Calvert, M., Cardamone, M., Moulton, M., and Ferguson, S. W., "Rotorwash Operational Footprint Modeling," Tech. rep., Missile Research Development and Engineering Center Redstone Arsenal AL Missile Guidance directorate, 2014.
- [2] Silva, M., and Riser, R., "CH-47D tandem rotor outwash survey," *AHS 67th Annual Forum, Virginia Beach, Virginia, USA*, 2011, p. 221.
- [3] Garcia-Dorado, I., Aliaga, D. G., Bhalachandran, S., Schmid, P., and Niyogi, D., "Fast Weather Simulation for Inverse Procedural Design of 3D Urban Models," *ACM Transactions on Graphics (TOG)*, Vol. 36, No. 2, 2017, p. 21.
- [4] D'Andrea, A., and Scorcelletti, F., "Enhanced numerical simulations of helicopter landing maneuvers in brownout conditions," *American Helicopter Society International 66th Annual Forum Proceedings, Phoenix, AZ*, 2010.

- [5] Taskgroup, R., “Rotary-wing brownout mitigation: technologies and training,” *Tech. Rep. RTO-TR-HFM-162, NATO Sci. Technol. Org.*, 2010.
- [6] Mapes, P., Kent, R., and Wood, R., “DoD helicopter mishaps FY85-05: findings and recommendations,” *US Air Force*, 2008.
- [7] Lee, T. E., Leishman, J. G., and Ramasamy, M., “Fluid dynamics of interacting blade tip vortices with a ground plane,” *Journal of the American Helicopter Society*, Vol. 55, No. 2, 2010, pp. 22005–22005.
- [8] Milluzzo III, J. I., and Leishman, J. G., “Vortical sheet behavior in the wake of a rotor in ground effect,” *AIAA Journal*, Vol. 55, No. 1, 2016, p. 24.
- [9] CAA, “CAP 490: Manual of Air Traffic Services Part 1,” 2015.
- [10] Steijl, R., Barakos, G., and Badcock, K., “A framework for CFD analysis of helicopter rotors in hover and forward flight,” *International journal for numerical methods in fluids*, Vol. 51, No. 8, 2006, pp. 819–847.
- [11] Lawson, S., Woodgate, M., Steijl, R., and Barakos, G., “High performance computing for challenging problems in computational fluid dynamics,” *Progress in Aerospace Sciences*, Vol. 52, 2012, pp. 19–29.
- [12] Osher, S., and Chakravarthy, S., “Upwind schemes and boundary conditions with applications to Euler equations in general geometries,” *Journal of Computational Physics*, Vol. 50, No. 3, 1983, pp. 447–481.
- [13] Roe, P. L., “Approximate Riemann solvers, parameter vectors, and difference schemes,” *Journal of computational physics*, Vol. 43, No. 2, 1981, pp. 357–372.
- [14] Van Leer, B., “Towards the ultimate conservative difference scheme. V. A second-order sequel to Godunov’s method,” *Journal of computational Physics*, Vol. 32, No. 1, 1979, pp. 101–136.
- [15] Van Albada, G., Van Leer, B., and Roberts, W., “A comparative study of computational methods in cosmic gas dynamics,” *Upwind and High-Resolution Schemes*, Springer, 1997, pp. 95–103.
- [16] Jarkowski, M., Woodgate, M., Barakos, G., and Rokicki, J., “Towards consistent hybrid overset mesh methods for rotorcraft CFD,” *International Journal for Numerical Methods in Fluids*, Vol. 74, No. 8, 2014, pp. 543–576.
- [17] Steijl, R., and Barakos, G., “Sliding mesh algorithm for CFD analysis of helicopter rotor–fuselage aerodynamics,” *International journal for numerical methods in fluids*, Vol. 58, No. 5, 2008, pp. 527–549.
- [18] Menter, F. R., “Two-equation eddy-viscosity turbulence models for engineering applications,” *AIAA journal*, Vol. 32, No. 8, 1994, pp. 1598–1605.
- [19] “Vertipedia,” <https://vertipedia.vtol.org/>, Accessed: 23-09-2019.
- [20] Alfred, J., Celi, R., and Leishman, J. G., “Flight Path Optimization for Brownout Mitigation Using a High-Fidelity Simulation Model,” *Journal of the American Helicopter Society*, Vol. 62, No. 3, 2017, pp. 1–15.
- [21] Wachspress, D., Whitehouse, G., Keller, J., Yu, K., Gilmore, P., Dorsett, M., and McClure, K., “A high fidelity brownout model for real-time flight simulations and trainers,” 2009, pp. 278–301.
- [22] Phillips, C., Kim, H. W., and Brown, R. E., “The flow physics of helicopter brownout,” *66th American Helicopter Society Forum: Rising to New Heights in Vertical Lift Technology*, 2010.
- [23] Ghosh, S., Lohry, M. W., and Rajagopalan, R. G., “Rotor configurational effect on rotorcraft brownout,” *28th AIAA Applied Aerodynamics Conference*, 2010, p. 4238.
- [24] Bagnold, R., “The physics of blown sand and desert dunes. London: Methuen.” 1941.
- [25] Greeley, R., and Iversen, J. D., *Wind as a geological process: on Earth, Mars, Venus and Titan*, Vol. 4, CUP Archive, 1987.
- [26] Shao, Y., and Lu, H., “A simple expression for wind erosion threshold friction velocity,” *Journal of Geophysical Research: Atmospheres*, Vol. 105, No. D17, 2000, pp. 22437–22443.
- [27] Syal, M., Govindarajan, B., and Leishman, J., “Mesoscale sediment tracking methodology to analyze brownout cloud developments,” *66th Annual Forum of the American Helicopter Society, Phoenix, AZ*, 2010, pp. 11–13.
- [28] Kutz, B., Günther, T., Rumpf, A., and Kuhn, A., “Numerical examination of a model rotor in brownout conditions,” 2014, pp. 2450–2461. Cited By 9.

- [29] Crowe, C. T., Schwarzkopf, J. D., Sommerfeld, M., and Tsuji, Y., *Multiphase flows with droplets and particles*, CRC press, 2011.
- [30] Tanner, P. E., "Photogrammetric characterization of a brownout cloud," *67th Annual Forum of the American Helicopter Society, Virginia Beach, VA*, 2011.
- [31] Amdahl, G. M., "Validity of the single processor approach to achieving large scale computing capabilities," *Proceedings of the April 18-20, 1967, spring joint computer conference*, 1967, pp. 483–485.
- [32] Rovere, F., Barakos, G., and Steijl, R., "CFD validation of a micro-rotor in ground effect," *45th European Rotorcraft Forum, Warsaw, CFAS*, 2019.
- [33] Kalra, T. S., Lakshminarayan, V. K., and Baeder, J. D., "Cfd validation of micro hovering rotor in ground effect," *American Helicopter Society 66th Annual Forum Proceedings, Phoenix, Arizona USA, Citeseer*, 2010.
- [34] Hunt, J. C., Wray, A. A., and Moin, P., "Eddies, streams, and convergence zones in turbulent flows," 1988.